

Inelastic spin-wave beam scattering by edge-localized spin waves in thin ferromagnetic film

Pawel Gruszecki,^{1,*} Konstantin Y. Guslienko,^{2,3} Igor L. Lyubchanskii,^{4,5} and Maciej Krawczyk¹

¹*Institute of Spintronic and Quantum Information, Faculty of Physics,
Adam Mickiewicz University, 61-614 Poznan, Poland*

²*Division de Fisica de Materiales, Depto. Polimeros y Materiales Avanzados: Fisica,
Química y Tecnología, Universidad del País Vasco, UPV/EHU, 20018 San Sebastian, Spain*

³*IKERBASQUE, the Basque Foundation for Science, 48009 Bilbao, Spain*

⁴*Donetsk Institute for Physics and Engineering named after O. O. Galkin (branch
in Kharkiv) of the National Academy of Sciences of Ukraine, 03028 Kyiv, Ukraine*

⁵*Faculty of Physics, V. N. Karazin Kharkiv National University, 61022 Kharkiv, Ukraine*

(Dated: May 17, 2022)

Spin waves are promising chargeless information carriers for the future, energetically efficient beyond-CMOS systems. Among many advantages there are the ease of achieving nonlinearity, the variety of possible interactions, and excitation types. Although the rapidly developing magnonic research has already yielded impressive realizations, multi-mode nonlinear effects, particularly propagating waves and their nanoscale realizations, are still an open research problem. We study theoretically the dynamic interactions of the spin waves confined to the edge of a thin ferromagnetic film with the spin-wave beam incident at this edge. We found the inelastically scattered spin-wave beams at frequencies increased and decreased by the frequency of the edge spin-wave relative to the specularly reflected beam. We observed a strong dependence of the angular shift of the inelastic scattered spin-wave beam on the edge-mode frequency, which allowed us to propose a magnonic demultiplexing of the signal encoded in spin waves propagating along the edge. Since dynamic magnetostatic interactions, which are ubiquitous in the spin-wave dynamics, are decisive in this process, this indicates the possibility of implementing the presented effects, also in other configurations and their use in magnonic systems.

I. INTRODUCTION

Nonlinear interactions are ubiquitous in nature and are indispensable in information processing devices, regardless of the carrier used for coding. The nonlinearity of spin-wave (SW) dynamics has long attracted the attention of researchers, and the topic is still very relevant in the emerging field of magnonics; see Refs. [1–7] and references therein. Among the many nonlinear effects that have been examined for application in magnonics is the decrease in the static magnetization component with increasing excitation power and the correlated change in SW frequency.⁸ The process of parametric pumping has been explored as a promising tool for the amplification of SWs, but it still awaits a suitable method for its integration, a necessary step in the construction of magnonic circuits. There are also other multiple-wave types of interaction between SWs, involving waves of the same origin, such as surface magnetostatic SWs^{9,10} and dipole-exchange SWs,¹¹ allowing for generation of second and third harmonics. A number of studies have been devoted to the investigation of three- and four-magnon collision processes, with different aspects of the nonlinear SW interactions being considered and various possible applications proposed.^{9–22} There have also been spectacular achievements in this area, such as Bose–Einstein condensation of magnons at room temperature and the demonstration of a pure magnon transistor.^{23,24}

Interactions between waves of different nature allow for transfer and control of dynamics in distinct subsys-

tems, such as chiral emission of SWs by a gyrotropic mode of skyrmion²⁵ or interaction between propagating bulk SWs (B-SWs) and domain-wall oscillations. Domain walls are considered as channels for SWs, suitable for guiding waves even along curved and very narrow paths, and therefore, they have attracted much attention,²⁶ also regarding nonlinear effects. In particular, the three-magnon interaction in a thin ferromagnetic film between an incident SW of frequency f_0 and the domain-wall flexure oscillations at frequency ν where investigated²⁷. As a result of this interaction, the SWs are scattered at frequencies $f_0 + \nu$ and $f_0 - \nu$, thus this phenomenon can be considered as an inelastic scattering of SWs (ISSW) on domain-wall oscillations. This effect is analogous to the Brillouin light scattering (BLS) by SWs,^{20,28} with the incident and scattered electromagnetic waves replaced by SWs, and the SWs replaced by domain-wall²⁷ or skyrmion²⁹ oscillations. In Ref. [30], a three-magnon process was also proposed as a tool to infer the information guided by SWs along the domain wall. Wang *et al.* proposed to use a three-magnon interaction between incident plane B-SWs and an SW confined in a region with Dzyaloshinskii-Moriya interaction as a tool to determine the strength of the Dzyaloshinskii-Moriya interaction.

From the points of view of both fundamental physics and applications, SWs located at edges or interfaces in planar structures are of particular interest. The edge confinement can be due to topological protection, wave properties, or a nonuniformity of the internal fields.^{31–34} In a finite structure with a magnetization component normal

to the film edge, surface magnetic charges create a static demagnetizing field. Suppose a sample is not ellipsoidal in shape. In that case, the demagnetizing field is nonuniform and forms wells in the internal magnetic field that is suitable for confining low-frequency SW oscillations, called edge SWs (E-SWs).^{35,36} In the case of a thin semi-infinite film or a waveguide with an in-plane external magnetic field directed perpendicularly to the edge, the demagnetizing field creates wells, enabling guidance of the SWs along the edge.^{37–39} However, neither the nonlinear interactions of B-SWs with bulk E-SW beams nor the exchange of energy and information between these two types has yet been investigated.

In the paper, we investigate the inelastic scattering of B-SWs by E-SWs in a thin ferromagnetic film through an analytical description and micromagnetic simulations. We analyze the interaction of an obliquely incident B-SW beam (frequency f_0) with the E-SWs (frequency ν) and find secondary B-SW beams at frequencies $f_0 - \nu$ and $f_0 + \nu$. We show that dipolar interactions are responsible for the nonlinearity related to the three-magnon process. The described effects are promising for the extension to other types of E-SWs. Interestingly, we observe that the angular shifts between the elastically reflected B-SW beam and the inelastically scattered B-SW beams are dependent on frequency. A clear explanation of this effect is obtained on the basis of energy and momentum conservation laws supplemented with the isofrequency contour analysis. Subsequently, we propose an application of inelastic three-magnon scattering to demultiplex information carried by E-SWs at different frequencies. Finally, we analyze the efficiency of B-SW scattering at the edge SWs and show that the efficiency of the assisted splitting (also known as stimulated splitting)^{30,40} is significantly greater than the confluence process. Because the proposed effect shall exist in a basic thin-film geometry, it is feasible for experimental demonstration and can have various applications in magnonics, such as in nonlinear magnonic nano-ring resonators,⁸ nonlinear SW interferometers for power-selective suppression of pulsed microwave signals,⁴¹ nonlinear SW logic gates,⁴² or omnidirectional SW array antennas.⁴³

The paper is organized as follows. In Sec. II, we describe the system under investigation. In Sec. III we introduce the analytical description of inelastic scattering of SWs. Then, in Sec. IV, we present the results of micromagnetic simulations and analyze the efficiency of B-SW scattering. Finally, we summarize our results in Sec. V. The appendix with details of micromagnetic simulations is placed at the end of the paper.

II. PROBLEM FORMULATION

We consider a reflection of the SW beam from the permalloy Py ($\text{Ni}_{80}\text{Fe}_{20}$) film edge under oblique incidence. The thin Py film (the saturation magnetization $M_s = 800$ kA/m and the exchange constant

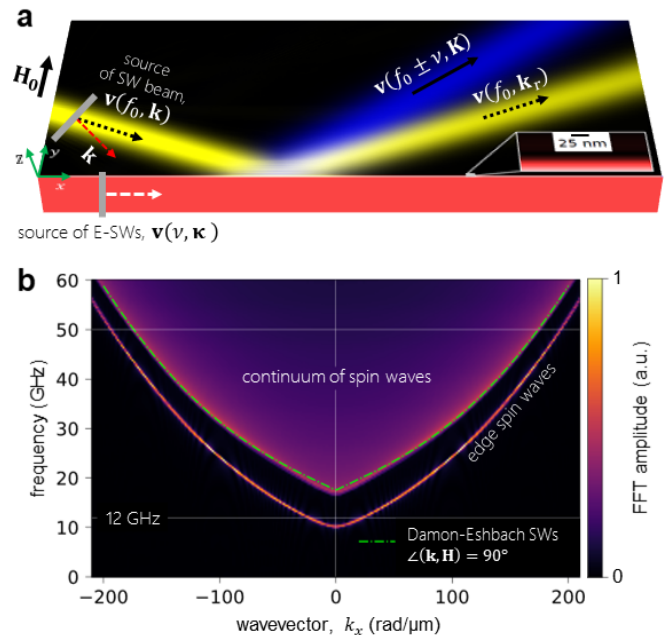


Figure 1. (a) Schema of the system under investigation. The red (at the edge), yellow, and blue (beams) colors correspond to the spin waves at frequencies ν (E-SW), f (incident and reflected B-SW), and $f \pm \nu$ (inelastically scattered SWs), respectively. The white color denotes areas where at least two frequencies are mixed. The black arrows represent the group velocities related to the incident and scattered beams, whereas the dashed red arrow represents the wavevector of the incident wave. The yellow arrow represents the E-SW. (b) Simulated dispersion relation (colormap in the background, where the color intensity corresponds to the averaged in space power related to the x component of the wavevector) with well visible E-SW band at frequencies downshifted with respect to the continuum of the B-SW band (highlighted area). The dispersion of the B-SW mode with the wavevector perpendicular to the static magnetization, i.e., Damon-Eshbach mode, is marked by the green dash-dotted line.

$A = 13$ pJ/m) of thickness $L = 10$ nm is magnetized by the external magnetic field $\mathbf{H}_0 = H_0 \hat{y}$ of the value $B_0 = \mu_0 H_0 = 0.3$ T (where μ_0 is the permeability of vacuum), directed perpendicularly to the film's edge, to the (x, z) plane, see Fig. 1(a). In this configuration, the static demagnetizing field gradually decreases the value of the static component of the effective magnetic field $\mathbf{H}_{\text{eff},y}$ at the vicinity of the film's edge, forming a suitable condition for a localization of the edge SWs^{44,45}.

A. Spin wave dynamics in thin films

In the micromagnetic approach the magnetization dynamics in a ferromagnetic film is described by the Landau-Lifshitz-Gilbert (LLG) equation of motion for

the magnetization vector \mathbf{M} ⁴⁶:

$$\frac{d\mathbf{M}}{dt} = -\frac{|\gamma|\mu_0}{1+\alpha^2}\mathbf{M}\times\mathbf{H}_{\text{eff}} - \frac{\alpha|\gamma|\mu_0}{M_S(1+\alpha^2)}\mathbf{M}\times(\mathbf{M}\times\mathbf{H}_{\text{eff}}), \quad (1)$$

where α is the damping parameter, γ is the gyromagnetic ratio and \mathbf{H}_{eff} is the effective magnetic field. The first term on the right side of the LLG equation describes the precession of the magnetization around the effective magnetic field direction, whereas the second term introduces damping to that precession. In our study, the effective magnetic field consists of the external magnetic field \mathbf{H}_0 , the exchange field \mathbf{H}_{ex} and the magnetostatic field \mathbf{H}_m : $\mathbf{H}_{\text{eff}} = \mathbf{H}_0 + \mathbf{H}_{\text{ex}} + \mathbf{H}_m$.

We use the open-source software MuMax3⁴⁷ to solve numerically Eq. (1) and simulate an inelastic scattering of the SW beam from the Py film edge. The details of simulations including beam generation and post-processing are presented in Appendix A.

B. Dispersion relation in thin ferromagnetic film

In the case of a uniformly in-plane magnetized thin film of a thickness L , under linear approximation and free boundary conditions on the dynamic components of the magnetization at its surfaces, the dispersion relation for the SW propagating in the film plane is given by^{48,49}:

$$f(\mathbf{k}) = \frac{1}{2\pi}\sqrt{\omega_0(\omega_0 + \omega_M F(\varphi, k))}, \quad (2)$$

where $\mathbf{k} = (k_x, k_y)$ is the two-dimensional wavevector, $\omega_M = \gamma\mu_0 M_s$, $\omega_0 = |\gamma|(B_0 + l_{\text{ex}}^2\omega_M k^2)$, $l_{\text{ex}} = \sqrt{2A/(\mu_0 M_s^2)}$ being the exchange length, and φ is the angle between the wavevector and the external magnetic field. The function $F(\varphi, k)$ is defined as:

$$F(\varphi, k) = 1 - P(kL)\cos^2\varphi + \frac{M_s P(kL)[1 - P(kL)]}{B_0\mu_0^{-1} + M_s l_{\text{ex}}^2 k^2}\sin^2\varphi,$$

where $P(\xi) = 1 - [1 - \exp(-\xi)]/\xi$.

Using Eq. (2), one may find isofrequency contours of the dispersion relation that are slices of the dispersion relation at a particular SW frequency over the (k_x, k_y) wavevector plane. These isofrequency contours will be used in the analysis of the allowed wavevectors of the scattered waves.⁵⁰

The direction of the wave energy flow is defined by the direction of the group velocity \mathbf{v}_g :

$$\mathbf{v}_g(\mathbf{k}) = \nabla_{\mathbf{k}}\omega(\mathbf{k}), \quad (3)$$

where $\omega(\mathbf{k}) = 2\pi f(\mathbf{k})$ is the dispersion relation defined in Eq. (2) and $\nabla_{\mathbf{k}} = [\partial/\partial k_x, \partial/\partial k_y]$ is a gradient in the wavevector space. Therefore, the direction of the SW group velocity is normal to the isofrequency contour for a given \mathbf{k} . Importantly, the direction of the group velocity can be equated with the direction of propagation of

the SW beam, i.e., its ray. For an isotropic media the isofrequency contours are circular and \mathbf{v}_g is parallel to \mathbf{k} , whereas, for anisotropic media, a typical situation for SWs in an in-plane magnetized thin film, the SW beam may propagate in a different direction than its wavevector points.

For the film thickness $L = 10$ nm and the considered frequency range the variation of the dynamical components of the magnetization along the z -axis is negligible.

C. Spin waves in semi-infinite thin film

The simulated dispersion relation, i.e., the SW frequency vs. the x component of the wavevector, is presented in Fig. 1(b). The dispersion relation shows the continuum of B-SW band starting at frequency $f \sim 20$ GHz (highlighted area) and an isolated SW band at smaller frequencies starting at ~ 10.8 GHz. The edge of the continuum B-SW for large k_x values is determined by the Damon-Eshbach mode, it is when $\mathbf{k} \perp \mathbf{H}_0$ (propagating far from the edge), and it is marked by the green dash-dotted line. At a small k_x the edge of the band is determined by the waves propagating along the magnetic field direction.⁴⁹

The isolated band at downshifted frequencies in Fig. 1(b) corresponds to an SW localized at the film's edge that propagates along the edge with the wavevector $\kappa \perp \mathbf{H}_0$. Its confinement, together with the lowered frequencies with respect of B-SW, enables a selective, and independent excitation of the B-SW beam at $f_0 > 20$ GHz and E-SW at $\nu \in (10.8, 20)$ GHz, i.e., at different frequencies in the same system. Thus, it is a well suitable system to answer the basic question of this study: Is it possible to scatter the incident B-SW beam on the E-SWs and excite B-SW beams at frequencies $f_0 \pm \nu$, as it is schematically shown in Fig. 1(a)? We answer this question, firstly developing an analytical model of the inelastic B-SW scattering on E-SW, and subsequently conducting detailed micromagnetic simulations.

III. MODEL OF INELASTIC SCATTERING OF SPIN WAVES

We have shown that in our system the two kinds of SW excitations can exist (Fig. 1): 1) the plane B-SWs, incident and scattered, in the bulk of the film, and 2) the E-SW localized at the film edge. This allows us to consider the nonlinear scattering of B-SWs on E-SWs as a three-magnon process and, therefore, to develop the analytical model.

We describe the unit magnetization vector $\mathbf{m}(\Theta, \Phi) = \mathbf{M}/M_s$ by the spherical angles Θ and Φ . Then, the magnetic free energy is $W = \int_V dV w$, with the energy density w integrated over the ferromagnet volume V defined in

the following form:

$$w = A \left[(\nabla\Theta)^2 + \sin^2\Theta(\nabla\Phi)^2 \right] - \mu_0 \mathbf{M} \cdot \mathbf{H}_0 - \frac{\mu_0}{2} \mathbf{M} \cdot \mathbf{H}_m. \quad (4)$$

To study magnetization dynamics we use the Landau-Lifshitz equation in the form suggested by Slonczewski⁵¹:

$$M_s \dot{\Phi} \sin\Theta = \gamma \left(\frac{\delta w}{\delta \Theta} \right), \quad M_s \dot{\Theta} \sin\Theta = -\gamma \left(\frac{\delta w}{\delta \Phi} \right), \quad (5)$$

where an overdot denotes the derivative with respect to time.

The SWs are defined as small perturbations on the magnetization background (in general, the magnetization background can be inhomogeneous and dynamical). The magnetization can be written as a sum of the static \mathbf{m}_0 and a small SW contribution \mathbf{m}_{sw} : $\mathbf{m} = \mathbf{m}_0 + \mathbf{m}_{\text{sw}}$. Analogously, the SW angles are defined as small deviations from the equilibrium magnetization angles $\Theta = \Theta_0 + \vartheta$, and $\Phi = \Phi_0 + \psi$. We assume that the equilibrium magnetization is parallel to the bias magnetic field and perpendicular to the film edge plane, thus $\mathbf{m}_0(\Theta_0, \Phi_0) = -\hat{y}$, $\Theta_0 = \pi/2$, and $\Phi_0 = -\pi/2$ (see, Fig. 1a). The components of the SW magnetization in quadratic approximation are $\mathbf{m}_{\text{sw}} = (\psi, \vartheta^2/2 + \psi^2/2, -\vartheta)$.

The inelastic scattering of incident/reflected plane B-SWs by the E-SW is determined by an interaction Hamiltonian H_{int} . It contains cubic terms of the SW amplitudes and other high-order interaction terms. We follow below the calculation scheme first suggested by Suhl⁵², who considered the problem of the parallel SW pumping in a bulk sample, as an interaction of the uniform precession magnon with the finite-wavevector SWs.

Accounting the decompositions $\mathbf{m} = \mathbf{m}_0 + \mathbf{m}_{\text{sw}}$ and $\mathbf{H}_m = \mathbf{H}_m^0 + \mathbf{h}_m$ into the static and dynamical parts, the system of Eqs. (5), keeping only the linear and quadratic terms in the SW magnetization angles, becomes

$$\begin{aligned} \frac{1}{\gamma} \dot{\psi}(\boldsymbol{\rho}) &= -\frac{2A}{M_s} \nabla^2 \vartheta(\boldsymbol{\rho}) - \mu_0 H_{m,y}^0 \vartheta(\boldsymbol{\rho}) - \\ &\quad - \mu_0 M_s \int d\boldsymbol{\rho}' G_{zz} \vartheta(\boldsymbol{\rho}') \\ &\quad - \mu_0 M_s \vartheta(\boldsymbol{\rho}) \int d\boldsymbol{\rho}' G_{yx} \psi(\boldsymbol{\rho}'), \\ -\frac{1}{\gamma} \dot{\vartheta}(\boldsymbol{\rho}) &= -\frac{2A}{M_s} \nabla^2 \psi(\boldsymbol{\rho}) - \mu_0 H_{m,y}^0 \psi(\boldsymbol{\rho}) \quad (6) \\ &\quad - \mu_0 M_s \int d\boldsymbol{\rho}' G_{xx} \psi(\boldsymbol{\rho}') \\ &\quad - \frac{\mu_0}{2} M_s \int d\boldsymbol{\rho}' G_{xy} (\vartheta^2(\boldsymbol{\rho}') + \psi^2(\boldsymbol{\rho}')) \\ &\quad - \mu_0 M_s \psi(\boldsymbol{\rho}) \int d\boldsymbol{\rho}' G_{yx} \psi(\boldsymbol{\rho}'), \end{aligned}$$

where $G_{\alpha\beta} \equiv G_{\alpha\beta}(\boldsymbol{\rho}, \boldsymbol{\rho}')$ are the magnetostatic Green functions averaged over the film thickness and defined by Eqs. (19)-(21) of Ref. [53], and $\boldsymbol{\rho} = (x, y)$, $\boldsymbol{\rho}' = (x', y')$ are the position vectors. The symbol $H_{m,y}^0 = H_{m,y}^0(y)$ represents the static dipolar field within the film, averaged

over the x -, and the z -coordinates. The field strongly depends on the coordinate y only near the film edge, in the region with the width about of the film thickness.

It is evident from Eqs. (6) that neither the exchange nor Zeeman interaction do not contribute to the quadratic terms in the equations of motion. These quadratic terms are responsible for the interaction between the SWs and arise due to the non-local magnetostatic coupling. The interaction energy density $w_{\text{int}} = -M_s \mathbf{h}_m \cdot \mathbf{m}_{\text{sw}}$ can be explicitly written as

$$w_{\text{int}} = -\frac{\mu_0}{2} M_s^2 \left[\psi \int d\boldsymbol{\rho}' G_{xy} (\vartheta^2(\boldsymbol{\rho}') + \psi^2(\boldsymbol{\rho}')) + (\vartheta^2 + \psi^2) \int d\boldsymbol{\rho}' G_{yx} \psi(\boldsymbol{\rho}') \right]. \quad (7)$$

Finally, using the symmetry properties of the Green functions $G_{\alpha\beta}(\boldsymbol{\rho}, \boldsymbol{\rho}') = G_{\beta\alpha}(\boldsymbol{\rho}', \boldsymbol{\rho})$, the cubic interaction energy can be written in the form

$$W_{\text{int}} = -\mu_0 M_s^2 L \int d\boldsymbol{\rho} \left[\psi(\boldsymbol{\rho}) \int d\boldsymbol{\rho}' G_{xy} (\vartheta^2(\boldsymbol{\rho}') + \psi^2(\boldsymbol{\rho}')) \right]. \quad (8)$$

In general, we can decompose the complex dynamic magnetization $\Psi = \vartheta + i\psi$ in a series of the eigenfunctions $m_k(\boldsymbol{\rho})$ of the linear eigenvalue problem given by the linear part of the system of Eqs. (6)

$$\Psi(\boldsymbol{\rho}, t) = \sum_k a_k(t) m_k(\boldsymbol{\rho}), \quad (9)$$

where a_k is the SW eigenmode amplitude, than the SW interaction energy (8) can be written in the form

$$W_{\text{int}} = -\frac{1}{2i} \mu_0 M_s^2 L \sum_{k,k',k''} \left[B_{kk'k''} a_k a_{k'} a_{k''}^* - B_{kk'k''}^* a_k^* a_{k'}^* a_{k''} \right], \quad (10)$$

with the SW scattering amplitudes

$$B_{kk'k''} = \int d^2\boldsymbol{\rho} \int d^2\boldsymbol{\rho}' G_{xy} m_k(\boldsymbol{\rho}) m_{k'}(\boldsymbol{\rho}') m_{k''}^*(\boldsymbol{\rho}'). \quad (11)$$

The first term in Eq. (10) corresponds to the elementary SW confluence process, whereas the second one corresponds to the SW splitting process. Let us investigate in more detail the confluence process described by the amplitude given by Eq. (11). The SW splitting amplitude is just complex conjugate to the confluence amplitude.

In the system under investigation, there is a translation invariance along the film edge. Therefore, the wavevector component along the x -axis can be introduced. According to markings in Fig. 1, the index $k' = \kappa$ will describe the localized E-SW, $m_\kappa(x, y) = m_\kappa(y) \exp(i\kappa x)$, the

non-localized B-SW $m_{\mathbf{k}}(x, y) = m_{\mathbf{k}}(y) \exp(ik_x x)$ are described by the indices \mathbf{k} , and \mathbf{K} , for the incident and inelastic scattered wave, respectively. Although, the linear system of Eqs. (6) cannot be solved analytically, we can assume that the non-localized B-SWs described by the indices \mathbf{k} and \mathbf{K} can be approximated by the plane waves $m_{\mathbf{k}}(\boldsymbol{\rho}) = \exp(i\mathbf{k} \cdot \boldsymbol{\rho})$ with the in-plane wavevectors \mathbf{k} and \mathbf{K} . Let us use explicitly the SW eigenfunction dependence on x . The amplitude of the scattering from \mathbf{k} -state to \mathbf{K} -state via a localized $\boldsymbol{\kappa}$ -state, i.e., absorbing the E-SW, is

$$B_{\mathbf{k}\boldsymbol{\kappa}\mathbf{K}} = 2\pi \int_0^\infty dy dy' \times \left[g_{xy}(y, y'; -k_x) m_{\mathbf{k}}(y) m_{\boldsymbol{\kappa}}(y') m_{\mathbf{K}}^*(y') \delta(k_x + \kappa - K_x) \right], \quad (12)$$

where $\delta(\xi)$ is the Dirac delta function and the simplified Green function g_{xy} is

$$g_{xy}(y, y'; k) = -\frac{1}{2\pi} \int_{-\infty}^\infty dp \frac{kp}{k^2 + p^2} P(L\sqrt{k^2 + p^2}) e^{ip(y-y')}. \quad (13)$$

The amplitude given by Eq. (12) is calculated without any assumption about the y -dependence of the SW eigenfunctions. If we assume additionally that $m_{\mathbf{k}}(y) = \exp(ik_y y)$, then the scattering amplitude Eq. (12) is transformed to

$$B_{\mathbf{k}\boldsymbol{\kappa}\mathbf{K}} = -2\pi \delta(k_x + \kappa - K_x) \frac{k_x k_y}{k^2} P(kL) \times \int_0^\infty dy m_{\boldsymbol{\kappa}}(y) e^{i(k_y - K_y)y}. \quad (14)$$

The E-SW mode profiles $m_{\boldsymbol{\kappa}}(y)$, in principle, can be obtained from a solution of the linearized system of Eqs. (6) accounting for the static and dynamic dipolar fields. However, this is practically impossible to implement analytically (see, Refs. [54–56]). Therefore, we use a trial function for the low frequency edge eigenmode, $m_{\boldsymbol{\kappa}}(y)$, in the form $m_{\boldsymbol{\kappa}}(y) = \exp(-y/\Delta)$ and assume that the localization width Δ of the E-SW is about of several tens of nm. The drawback of this trial function is that it is not orthogonal to the plane SWs. Then, Eq. (14) yields to the scattering amplitude

$$B_{\mathbf{k}\boldsymbol{\kappa}\mathbf{K}} = -2\pi \Delta \delta(k_x + \kappa - K_x) \frac{k_x k_y}{k^2} P(kL) \times \chi((k_y - K_y)\Delta), \quad (15)$$

where the function $\chi(x) = (1 + ix)/(1 + x^2)$ reflects non-conservation of the y -component of the SW momentum due to breaking the translation invariance along the y -axis by the film edge.

If the SW beam is elastically reflected from the film edge and the Snell law is satisfied, we can accept that

$k_y = -k_{r,y}$ and $k_y - k_{r,y} = 2k_y$, but for the inelastic scattering the y -component of the scattered wave, K_y , needs to be extracted from the dispersion relation, Eq. (2). The SW confluence (absorption of E-SW by B-SW) amplitude given by Eqs. (14) and (15) is represented mainly by the incident SW wavevector components. The SW splitting (emission of E-SW by B-SW) amplitude is given by Eqs. (14), (15), where one has to substitute κ to $-\kappa$ and the function $\chi(x)$ to its complex conjugate. Note that the amplitude angular dependence is $B_{\mathbf{k}\boldsymbol{\kappa}\mathbf{K}} \propto \sin(2\varphi) \chi((k_y - K_y)\Delta)$, where φ is already defined angle of incidence being counted from the y -axis, $k_y < 0$ and $K_y > 0$. The function $B_{\mathbf{k}\boldsymbol{\kappa}\mathbf{K}}(\varphi)$ reaches its maximum at $\varphi = \pi/4$ if the E-SW mode localization is strong with respect to the wavelengths of incident and scattered waves, i.e., $(k_y - K_y)\Delta \ll 1$. The scattering amplitude becomes negligibly small in the opposite limiting case of weakly localized E-SW, $(k_y - K_y)\Delta \gg 1$.

The scattering amplitude $B_{\mathbf{k}\boldsymbol{\kappa}\mathbf{K}}(\varphi)$ accounts explicitly for the momentum conservation law

$$K_{x,\pm} = k_x \pm \kappa \quad (16)$$

along the film edge. From the other side, the energy conservation law

$$\omega_{\mathbf{K},\pm} = \omega_{\mathbf{k}} \pm \omega_{\boldsymbol{\kappa}} \quad (17)$$

should be satisfied for the confluence (+) and splitting (−) processes, where $\omega_{\mathbf{k}} = 2\pi f_0$ and $\omega_{\boldsymbol{\kappa}} = 2\pi\nu$. Therefore, the confluence and splitting amplitudes depend on the final plane B-SW wavevector \mathbf{K} and the x -component of the E-SW vector, $\boldsymbol{\kappa}$. Assuming the plane wave approximation $m_{\mathbf{k}}(\boldsymbol{\rho}) = \exp(i\mathbf{k} \cdot \boldsymbol{\rho})$ for the non-localized B-SW and neglecting the static dipolar field $H_{m,y}^0$, the linearized system of Eqs. (6) can be essentially simplified yielding the well-known SW dispersion relation of an infinite film with thickness L , defined in Eq. (2).

IV. RESULTS AND DISCUSSION

1. Analysis of B-SW beam scattering by E-SW

To demonstrate the inelastic scattering of B-SWs on E-SW we conducted micromagnetic simulations. In Fig. 2(a) we show the frequency spectrum calculated for the SW beam excited at the frequency $f_0 = 50$ GHz with the wavevector \mathbf{k} directed under the angle of incidence $\varphi = 30^\circ$ that falls at the film's edge, where an independently excited the E-SW at frequency $\nu = 12$ GHz independently propagates along the x -axis with $\kappa > 0$.

The first signature of ISSW is the presence of a series of peaks in Fig. 2(a). The two most pronounced peaks correspond to the frequencies $f_0 = 50$ GHz and $\nu = 12$ GHz, i.e., to the excited and elastically reflected B-SW, and E-SW, respectively. There is also a peak at $2\nu = 24$ GHz related to the second-harmonic generation

by the E-SW. The process of second-harmonic generation of plane waves by the E-SW has been already described in detail in Refs. [45 and 57], here, however, we focus on an inelastic scattering. The two other peaks marked in Fig. 2(a), at the frequencies $f_0 - \nu = 38$ GHz and $f_0 + \nu = 62$ GHz, correspond exactly to the ISSWs, accordingly with the energy conservation law, Eq. (17). Namely, these peaks correspond to the splitting and confluence processes, respectively. Interestingly, the amplitude of the wave generated in the splitting process is greater than in the confluence process, pointing at a higher efficiency of the splitting than the confluence process. Moreover, the occurrence of a peak at the $f_0 - \nu$ frequency indicates, the emission of the E-SW at a frequency ν in the splitting process. It suggests that an already existing E-SW at frequency ν triggers this process. Instead of having a three-SW splitting with random wave excited, we observe the assisted splitting process, also known in the literature as a stimulated splitting process^{30,40}].

Let us analyze the SW beams shown in Fig. 2(b)-(d) corresponding to the detected frequencies. At the frequency f_0 there are two beams that propagate towards and outwards the interface, namely, the incident beam and the reflected beam [Fig. 2(b)]. These beams at frequencies $f_0 \pm \nu$, presented in Fig. 2(c) and (d), propagate only outward the film's edge, thus, confirming their excitation at the film's edge as a result of the ISSW. In Fig. 2(b)-(d), we plot also the beam rays (solid lines along the beams), which are associated with the direction of the group velocity. All the beams propagate under very close angles, namely, the elastically reflected beam

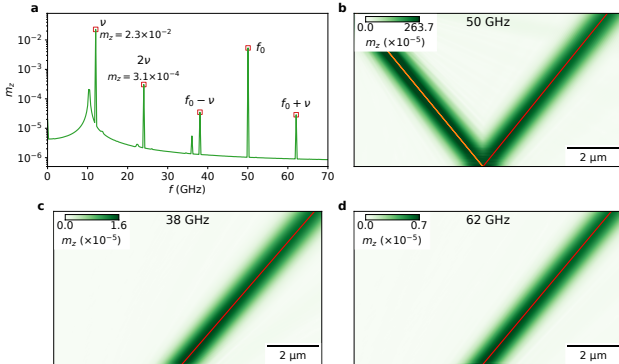


Figure 2. (a) The spectrum of SWs with the most prominent frequency peaks corresponding to the E-SWs (ν), 2nd harmonic generated SWs ($2\nu = 24$ GHz), SW beam of frequency $f_0 = 50$ GHz, and the inelastically scattered SW beams $f_0 \pm \nu$ at the frequencies of 38 and 62 GHz. (b) The intensity map of the incident and reflected SW beams at frequency 50 GHz. (c) and (d) Intensity maps of SWs at frequency 38 GHz and 62 GHz, respectively. The angles of propagation of the scattered beams in (c) and (d) differ slightly with respect to each other and with respect to the primary reflected beam presented in (a). The locations of antennas exciting both, SW beam and E-SWs, are schematically shown in Fig. 1(a).

at frequency 50 GHz propagates under the angle of 39° , whereas the scattered beams at frequencies 38 GHz and 62 GHz, propagate under the angles of 41° and 40° , respectively. The difference in the beam ray directions of incident and reflected waves arises from the anisotropy of the isofrequency contour – see, the elliptical shape of the contours in Fig. 3. Hence, also the directions of the phase velocity (30°) and group velocity (39°) differ from each other.

In order to detect the values of wavevectors corresponding to the SWs and verify whether the momentum conservation law, Eq. (16), is fulfilled, we calculate spatial Fast Fourier Transform (FFT) for SWs at frequencies ν , f_0 , and $f_0 \pm \nu$. For the frequency $\nu = 12$ GHz we obtain the wavevector of value $\kappa = \hat{x}2\pi/(285 \text{ nm})$, i.e., the wavelength equal to 285 nm. The k -space maps of the FFTs for the other frequencies are shown in Fig. 3(a)-(c) by a grayscale colormaps in the background, there are the black spots corresponding to the considered SWs.

The k -space representation at the frequency f_0 [Fig. 3(b)] shows the two peaks corresponding to the incident and reflected beams, propagating with the negative and positive k_y , respectively. These two waves have the same tangential to the interface component of the wavevector, k_x , in agreement with the momentum conservation law for the wave reflection from the edge possessing translational symmetry. On the other hand, at $f_0 \pm \nu$ [Fig. 3(a) and (c)] there are visible single peaks at the positive k_y half-space. The tangential components of their wavevectors, K_x are shifted by κ with respect to k_x , in agreement with the momentum conservation laws defined in Eq. (16). Accordingly with the analytical predictions of Sec. III, we confirm that for $f = f_0 \pm \nu$ we get the scattered beam at the wavevector $\mathbf{K}_\pm = (k_x \pm \kappa, K_y)$, with the K_y -component allowing to satisfy the dispersion relation of the Py film $f(\mathbf{K})$, i.e., \mathbf{K} pointing at the isofrequency contour, exactly as demonstrated in Fig. 3(a) and (c). Interestingly, for the cases shown in Fig. 3(a)-(c), the mode profiles in k -space reveal that the angles of the phase velocities for the reflected and the two scattered beams are almost identical, and are 29.9° , 29.1° , and 31.5° , respectively.

The demonstration presented above opens up also other ways to use the three-magnon ISSW process. Namely, depending on the location of the source of E-SW in relation to the beam spot, i.e., the change of the κ sign, we can obtain a scattered beam propagating at different angles. Moreover, if we use a source of E-SW at both sides of the beam spot exciting a standing E-SW, we can obtain the two pairs of scattered beams at frequencies $f_0 + \nu$ and $f_0 - \nu$. Confirmation of such a scenario is displayed in Figs. 3(d), (e), and (f) where we show the SWs in the k -space at frequencies 38 GHz, 50 GHz, and 62 GHz, respectively, obtained from the scattering of the B-SW beam at 50 GHz on 12 GHz standing E-SW. It is visible, that at 38 GHz [Fig. 3(d)] and 62 GHz [Fig. 3(f)] the pair of black spots are present. The spots from the pair correspond to the two scattered beams propagat-

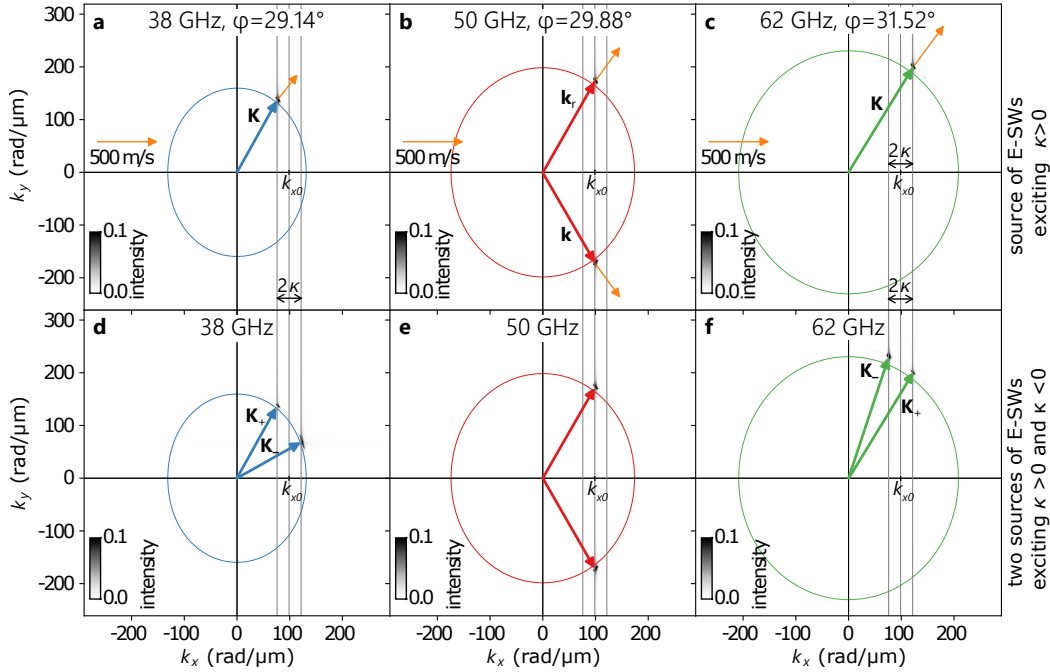


Figure 3. The momentum-space representation of the ISSW. The grayscale color map in the background represents the profile of SWs in the k -space obtained from simulations. The sharp black regions that are marked by the color arrows represent the profile of the wavevectors of the SW beams. In (a)-(c) are shown results obtained for the case from Fig. 2, where the source of E-SW is placed on the left side of the incident beam spot, whereas in (d)-(f) there are two sources of E-SWs located on both sides of the incident beam spot. In (a) and (c) are shown results for $f_0 - \nu = 38$ GHz, in (b) and (e) for 50 GHz – specular reflection, whereas in (c) and (f) for $f_0 + \nu = 62$ GHz. The solid ellipses represent isofrequency contours for corresponding frequencies resulting from the analytical dispersion relation, Eq. (2). The thin-orange arrows correspond to the group velocities obtained analytically for a given wavevector (their length notes the magnitude of \mathbf{v}_g). The angle $\varphi = \tan^{-1}(k_x/k_y)$ in (a)-(c) denotes the angle of the phase velocity with respect to the normal to the film edge.

ing under different angles, which are determined by the momentum conservation Eq. (16) for the x -component $K_{x,\pm} = k_x \pm \kappa$, and the y -components K_y matching with the isofrequency contour, independently at $f_0 + \nu$ and $f_0 - \nu$. Interestingly, the effect can be considered as a splitting of the ISSW into two beams.

2. Utilizing ISSW – SW demultiplexing

The $\mathbf{K}_{\pm} = (k_x \pm \kappa, K_y)$ dependence combined with the anisotropy of the SW dispersion, which varies with the frequency, makes it possible to obtain the frequency-dependent direction of the inelastically scattered SW beams. Such a behaviour can be used to spatially separate information carried by E-SWs at different frequencies, i.e., useful for SW demultiplexing or to design an SW nanoscale spectrum analyzer.⁵⁸ To achieve that, the angle of the inelastically scattered beam should strongly depend on the frequency of E-SW.

Interestingly, a slight modification of the previously studied system is enough to achieve such functionality, that is, to change the placement of the E-SWs source to the right side of the incident SW beam spot, see Fig. 4(a). In this case, the wavevector associated with the E-SWs

has the negative sign ($\kappa < 0$). Therefore, we expect the following pair of scattered beams: at frequency $f_0 - \nu$ with $K_x = k_x + |\kappa|$ and at $f_0 + \nu$ with $K_x = k_x - |\kappa|$. Isofrequency contour analysis shows that at $f_0 - \nu$ the direction of group velocity may significantly depend on the frequency of the E-SW ν . However, due to the requirement to preserve the tangential to the film edge component of the wavevector and the finite value of the frequency at $k = 0$, this process can only occur in a certain frequency range of E-SWs, i.e., for waves at frequencies greater than 10.8 GHz (the resonance frequency at $\kappa = 0$) and lower than 13 GHz, at which the condition $\max\{k_x(f - \nu)\} < k_x + |\kappa|$, still holds.

Taking these limitations into account, we perform simulations for a system in which SW beam at 50 GHz frequency (incidence at 30°) is scattered on E-SWs excited at 10.8 GHz, 11.4 GHz, 12.0 GHz, and 12.6 GHz. Results of simulations are displayed in Fig. 4(b), where scattered SWs at different frequencies are depicted by different colors. Indeed, depending on the frequency of the E-SW, the scattered SW beams propagate at easily distinguishable angles. For instance, the SW beam at frequency 39.2 GHz (red color) propagates at an angle around 33° with respect to the film edge, whereas the SW beam at frequency 37.4 GHz (yellow color) propagates at an angle

around 11° . It means that E-SWs in a narrow 1.8 GHz range of frequencies (from 10.8 to 12.6 GHz) excite SW beams propagating under the angles differing by 30° at frequencies from 37.4 up to 39.2 GHz. Such functionality may be important for SW demultiplexing and frequency converting systems of future magnonic signal processing devices.

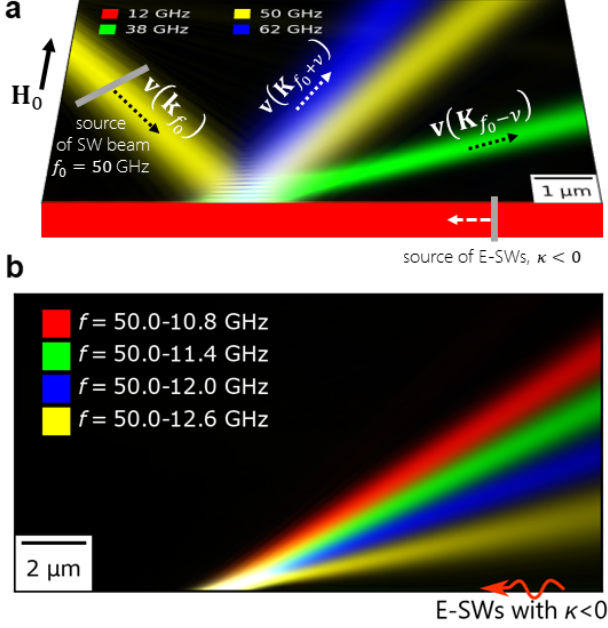


Figure 4. (a) The result of micromagnetic simulations showing the scattering of a 50 GHz B-SW beam (yellow color) incident at the angle of 30 degrees on a 12 GHz E-SW with $\kappa < 0$ (red color). Two scattered beams at 38 GHz (green) and 62 GHz (blue) propagate at significantly different angles to each other, and to the reflected beam. Areas, where excitation of the B-SW beam and E-SWs takes place, are schematically marked with gray lines. (b) SW beams at frequencies 39.2 GHz (red color), 38.6 GHz (green color), 38 GHz (blue color), and 37.4 GHz (yellow color) excited at the edge of ferromagnetic film as the result of SW beam (at 50 GHz) scattering at the E-SWs of frequencies 10.8 GHz, 11.4 GHz, 12.0 GHz, and 12.6 GHz, respectively.

3. Efficiency of the inelastic scattering process

Let us discuss now the efficiency of the inelastic scattering process and compare qualitatively the simulation results with the analytical predictions. According to the analytical model of the three-magnon scattering process developed in Sec. III, the amplitude of the scattered SW beam should linearly depend on the amplitude of both, the E-SW and the incident B-SW beam. In order to verify that, a set of micromagnetic simulations at different excitation amplitudes of the B-SW beam at frequency $f_0 = 50$ GHz and E-SWs at frequency $\nu = 12$ GHz, and

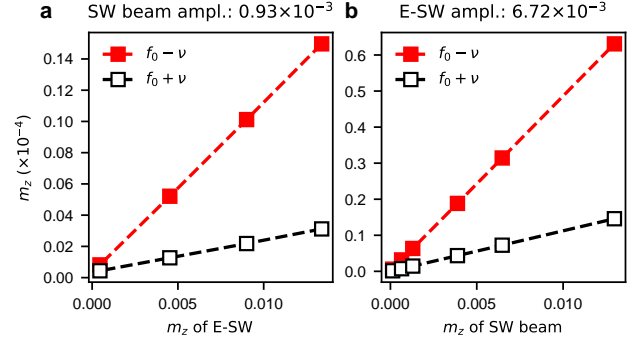


Figure 5. The amplitudes of the m_z component of magnetization of the inelastically scattered SWs at frequencies $f_0 \pm \nu$ for different amplitudes of m_z of the E-SW (a) and the B-SW beam (b). The results of simulations presented in (a) are obtained for the B-SW beam of amplitude equal to 0.93×10^{-3} , whereas the results presented in (b) are for the E-SW of the amplitude 6.72×10^{-3} .

$\kappa > 0$ is performed. Subsequently, the resulting amplitudes of the out-of-plane magnetization component, m_z , at the distance $y = 100$ nm from the film edge are analysed.

The SW amplitude of the two scattered beams at the frequencies $f_0 - \nu$ and $f_0 + \nu$ on the amplitude of E-SWs are presented in Fig. 5(a). These results are obtained for the scattering of B-SW beam of amplitude maximum equal to 0.93×10^{-3} at the excitation point. As predicted by the model, the resulting linear relationship is clearly visible. Further simulations also confirm the linear dependence of the amplitude of the scattered B-SW beam on the amplitude of the incident SW beam, see Fig. 5(b). These results are obtained at the E-SWs of amplitude equal to 6.72×10^{-3} . Interestingly, in both cases, the amplitude of SW beams at the frequency $f_0 - \nu$ (the splitting process) is greater and faster increases with the amplitude of E-SW, than the amplitude of SW beam at the frequency $f_0 + \nu$ (the convolution process). Moreover, the amplitudes of the scattered beams are only 2-3 orders smaller than the amplitudes of the incident SW beam or E-SW. Clearly, the three-magnon inelastic scattering process under investigation is a thresholdless one.

As the next step, let us examine the amplitude of the inelastically scattered B-SW beams in dependence on the angle of incidence. Here, we consider the scattering of B-SW beam at 50 GHz and 30 GHz on the E-SWs (12 GHz) of the amplitude 6.72×10^{-3} [the same as used in Fig. 5(b)].

In Fig. 6(a), (b), and (c) we show the SW-beam cross-section $|m_z(x)|$ along the x -axis at $y = 100$ nm for different angles of incidence (the different colors of lines) at 50 GHz – specular reflection, 38 GHz, and 62 GHz, respectively. Since, the amplitude of the scattered beams in the studied range of amplitudes linearly depends to the amplitude of both E-SW and the incident SW beam, the amplitudes for each simulation are normalized to the

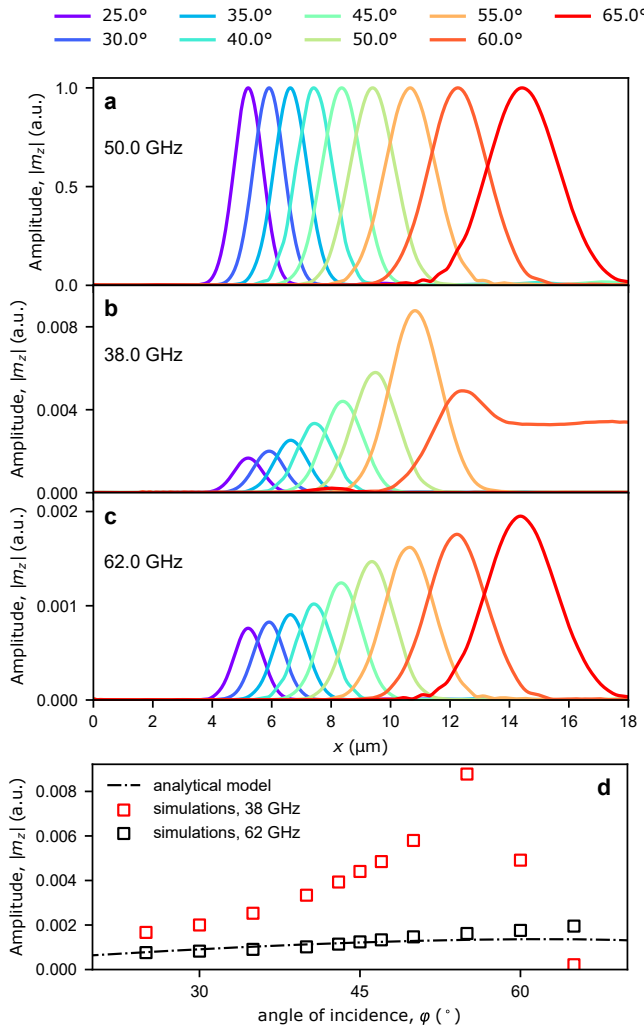


Figure 6. (a), (b), and (c) dependencies of the $|m_z|$ component of dynamic magnetization detected at $y = 100$ nm distance from the film edge for the reflection and inelastically scattered SWs at 50 GHz, 38 GHz, and 62 GHz, respectively. Different colours represent results at different angles of incidence of SW beam (50 GHz) falling at the edge, where E-SWs at frequency 12 GHz propagate along the $+x$ direction ($\kappa > 0$). The amplitudes are normalized to the amplitude of the elastically reflected beams at a given angle, i.e., $m_{\text{scattered}}(y = 100 \text{ nm})/m_{\text{reflected}}(y = 100 \text{ nm})$ where $m_{\text{scattered}}(y = 100 \text{ nm})$ and $m_{\text{reflected}}(y = 100 \text{ nm})$ are amplitudes of the scattered and reflected waves at $y = 100$. (d) The comparison of the results of micromagnetic simulations (the empty black and red squares) with the analytical model (dash dotted black line) for inelastically scattered waves is done using the function $|m_z| = C \sin(2\varphi) \chi((k_y - K_y)\Delta)$ with $\Delta = L = 10$ nm and $C = 1.4 \times 10^{-3}$.

SW amplitude of the elastically reflected beam. Thus, in Fig. 6(a), the amplitudes of all beams are equal 1, whereas, the amplitudes in Fig. 6(b), and (c) represent the relative value (see caption of the figure). It is visible, that with increasing the angle of incidence, the amplitudes of the scattered beams increase. Notewor-

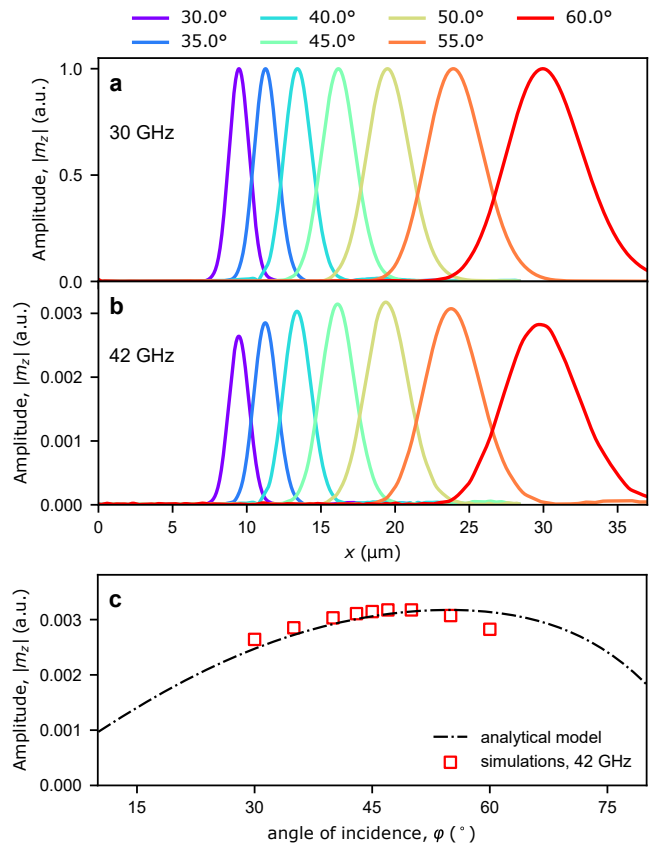


Figure 7. The dependencies of $|m_z|$ at $y = 100$ nm distance from the film edge at the specular reflection [(a) 30 GHz] and inelastic scattering SW [(b) 42 GHz] propagating outwards the edge. Different colours represent results at different angles of the SW beam incidence at the edge where E-SW at frequency 12 GHz propagate along the $+x$ direction. Similarly like in Fig. 6, the amplitudes are normalized to the amplitude of the elastically reflected beams at a given angle. (c) The comparison of the results of micromagnetic simulations (the empty red squares) with the analytical model (dash dotted black line) for inelastically scattered waves using the equation $|m_z| = C \sin(2\varphi) \chi((k_y - K_y)\Delta)$ with $\Delta = L = 10$ nm and $C = 3.2 \times 10^{-3}$.

thy, in the case of the scattered wave at the frequency $f_0 - \nu = 38$ GHz and for the angles of incidence greater than 55° the scattered SW beam is not observed. This is because at frequency 38 GHz there are no available solutions for the SW with a high value of K_x , i.e., at $f = f_0 - \nu$, $\max\{K\} < k_x - \kappa$.

At a lower frequency of the incident SW, i.e., 30 GHz, there are solutions only for $f_0 + \nu = 42$ GHz. The frequency $f_0 - \nu = 18$ GHz is only a bit larger than the bottom of the SW spectrum for B-SWs (16.5 GHz). Therefore, at the frequency 18 GHz only SWs with very small values of K_x , i.e., $K_x \ll k_x - \kappa$, can propagate. The results are shown in Fig. 7(a), and (b). The amplitude of the scattered beam reaches maximum for the angle of incidence equal 50° what is different result than in the

case of 50 GHz SW beam.

The obtained angular dependence can be directly compared with the data from the analytical model. Combining Eq. (15) with the dispersion relation, Eq. (2) one may numerically derive scattering efficiency $B_{\mathbf{k}\nu\mathbf{K}}$ in dependence on the incidence angle of the B-SW beam. The comparison for the SW beams at frequencies 50 GHz and 30 GHz are presented in Figs. 6(d) and 7(c), respectively. A good agreement for both cases for the confluence process ($f_0 + \nu$) is achieved. Furthermore, the amplitude of the scattered waves due to the confluence process is larger for 30 GHz waves. According to the analytical model, the better the localization, the more efficient the scattering should be. It agrees well with simulation results since the wavelength for 30 GHz is greater than for 50 GHz (33 nm for 50 GHz and 53 nm for 30 GHz), and therefore, for lower frequency, we get better localization. Moreover, according to the analytical model, the maximum of the scattering efficiency should shift towards the waves incident at the angle of 45 degrees for very well localized waves and for greater angles for poorer localization. This prediction also agrees with the simulation results

However, for the splitting process ($f_0 - \nu$) present at the 50 GHz incident SW beam, the simulated and calculated angular dependencies differ essentially. Overall, this means that although the analytical model describes the confluence process very well, it does not describe correctly the splitting process ($f_0 - \nu$) obtained in micromagnetic simulations. This is not surprising since the analytical model does not take into account the presence of E-SW triggering the process of three-SW splitting. Namely, the developed analytical model considered only three-SW splitting, not as in our case, assisted (stimulated) three-SW splitting.

V. CONCLUSIONS

We conducted a combined analytical and numerical study of the inelastic scattering of SW beam on the E-SW mode in the in-plane magnetized semi-infinite ferromagnetic film. We show that the scattering may lead to the appearance of the multiple SW beams at shifted frequencies related to the absorption and emission processes of the E-SW mode.

We presented the analytical model describing the three-magnon scattering process, which allows us to formulate the essential criteria of the E-SW mode absorption and emission, i.e., the energy and momentum conservation laws, and estimate the efficiency of the processes. Subsequently, we confirmed analytical predictions by micromagnetic simulations demonstrating the scattering of 50 GHz SW beam on the E-SWs at frequency 12 GHz in 10 nm thick Py film. We showed that the observed inelastic scattering is a three-magnon confluence or assisted (stimulated) splitting of the E-SW modes. Thus, the effect of the bulk-SW inelastic scattering on the E-

SWs can be treated as a magnonic analog of the Brillouin scattering of electromagnetic waves by SWs. Moreover, we found that the stimulated splitting process has considerably greater efficiency than the confluence process

Importantly, depending on the chosen conditions, the inelastically scattered beams can propagate at the same or different angles, then the elastically reflected SW beam. Based on the analysis of the isofrequency contours of SWs in the ferromagnetic film, we utilized the effect to demonstrate demultiplexing a signal carried by the E-SWs by separating spatially scattered SW beams at different frequencies. In contrast, the SW beam scattering by the standing E-SW can be used to split the signal into two beams.

The simplicity of the proposed system geometry and the linear dependence of the amplitude of the scattered SWs on the amplitudes of the E-SWs and the incident SW beam make the experimental realization feasible and promising for magnonic applications. The magnetostatic interactions being ubiquitous in ferromagnetic films and influencing SW dynamics to suggest the existence of the three-magnon processes between B-SW and other types of edge localized SWs. Thus, our findings are important contributions to understanding and utilizing the nonlinear phenomena in SW dynamics and the next step towards the realization of magnonic circuits.

ACKNOWLEDGMENTS

The research leading to these results has received funding from the National Science Centre of Poland, project no. 2019/35/D/ST3/03729. I.L. acknowledges support by COST action under project CA17123 MAGNETOFON. K.G. acknowledges support by IKERBASQUE (the Basque Foundation for Science). The work of K.G. was supported in part by the Spanish Ministerio de Ciencia e Innovacion grant PID2019-108075RB-C33/AEI/10.13039/501100011033. The simulations were partially performed at the Poznan Supercomputing and Networking Center (Grant No. 398).

DATA AVAILABILITY

The data that support the findings of this study are available from the corresponding author upon reasonable request.

Appendix A: Micromagnetic simulations

Micromagnetic simulations have been proven to be an efficient tool for the calculation of magnetization dynamics in ferromagnetic materials. Presented results were obtained using the code MuMax3⁴⁷, which solves time-dependent LLG Eq. (1) with included Landau-Lifshits damping term, by using the finite difference method. In

simulations, we considered an oblique SW beam propagation in Py thin film saturated by an in-plane magnetic field of value $\mu_0 H_0 = 0.3$ T oriented perpendicular to the film edge (see, Fig. 1). We assumed the typical magnetic parameters of Py ($\text{Ni}_{80}\text{Fe}_{20}$ alloy), i.e., the exchange stiffness constant $A = 13$ pJ/m, saturation magnetization $M_s = 800$ kA/m, gyromagnetic ratio $\gamma = 176$ rad GHz/T and the value of damping $\alpha = 0.0001$. The system of size $L_x \times L_y \times L_z$ is discretized with cuboid elements of dimensions $l_x \times l_y \times L_z$. Lateral dimensions of the single cell $l_x \times l_y = 5 \times 5$ nm² are slightly smaller than the exchange length of Py ($l_{\text{ex}} = 5.7$ nm). The lateral dimension of the system L_x and L_y are adjusted in such a way that the spin wave beams were clearly visible, e.g., in the case of 50 GHz SW beam incidence under angle of 30° what is most frequently used scenario $L_x = 20$ μm and $L_y = 10$ μm .

In the study we simulated a SW beam of width ca. 1 μm in its waist propagating under the angle of incidence 50° (the angle between the SW wave-vector \mathbf{k}_i and the y -axis). SW beams were excited by the microwave magnetic field of the Gaussian profile type described in Ref. [38]: $h_{\text{mf}}(x', y') = h_0 \text{Win}(wx') \exp\left[-\frac{(y'/(0.5L))^2}{2\sigma^2}\right]$ where h_0 is the amplitude of the field, Win is the Dirichlet window function, $w = 10$ nm is the width of the antennae, $L = 2500$ nm is its length, and $\sigma^2 = 0.1$.

The point-source of radius ca. 30 nm exciting E-SWs was located at the edge of the film at the left or/and right side of the beam spot in distance ca. 5 μm . At the borders of the simulated domain, different than the film's edge, the absorbing boundary conditions have been assumed⁵⁹.

The simulations consisted of three stages. In the first one a static magnetization configuration was obtained, then, the SWs (B-SW beam and E-SW) were continu-

ously excited until reaching a steady-state (typically we run simulations for 60 ns). Finally, the simulation results (m_z component of the magnetization) were stored with the sampling interval of 5 ps to the matrix: $m_z(t; x, y)$. The results obtained in such a way were next processed.

Postprocessing. In the first stage of postprocessing we calculated the pointwise fast Fourier transforms (FFT) over time of m_z component of magnetization sampled: $\tilde{m}_z(f; x, y) = \frac{2}{N} \mathcal{F}_t[m_z(t; x, y)]$, where \mathcal{F}_t denotes FFT operation over time implemented in NumPy^{60,61} and N is the number of samples processed. We have chosen the following sampling scheme providing frequency resolution $\delta f = 0.2$ GHz, i.e., we have used $N = 1200$ samples stored with sampling interval $t_{\text{sampl}} = 1/(N\delta f)$. The normalization $\frac{2}{N}$ together with the sampling scheme precisely resolving frequencies used in the study enabled us to precisely resolve the amplitudes of SWs after FFT. Namely, there is the same amplitude of the time-dependent signal of a given frequency as the absolute value of the peak corresponding to that frequency of the transformed signal. In all the further steps this matrix was processed.

SW spectrum. The SW spectra presented in Fig. 2 was obtained using the following formula $|m_z|(f) = \max(|\tilde{m}_z(x, y)|)(f)$. The amplitude corresponds to maximal amplitudes of spin waves at given frequency f present in the sample.

Mode profiles. Mode profiles for frequencies f_i presented in Fig. 2(b)-(d) were obtained using the formula $m_{z,f_i} = |\tilde{m}_z(f = f_i; x, y)|$.

Mode profiles in the k -space. The isofrequency map (mode profile in the k space) for frequency f_i can be derived from the SW mode profiles as a 2-dimensional-FFT: $IFM_{f_i}(k_x, k_y) = \left| \mathcal{F}_{x,y} \left[\text{Re} \left\{ \tilde{m}_z(f = f_i; x, y) \right\} \right] \right|$, where $\mathcal{F}_{x,y}$ denotes 2-dimensional FFT operation over the x and y coordinates.

* gruszecki@amu.edu.pl

¹ P. E. Wigen, *Nonlinear phenomena and chaos in magnetic materials* (World Scientific, 1994).

² M. G. Cottam, *Linear and nonlinear spin waves in magnetic films and superlattices* (World Scientific, 1994).

³ A. G. Gurevich and G. A. Melkov, *Magnetization oscillations and waves* (CRC Press, 1996).

⁴ S. A. Nikitov, D. V. Kalyabin, I. V. Lisenkov, A. N. Slavin, Y. N. Barabanenkov, S. A. Osokin, A. V. Sadovnikov, E. N. Beginin, M. A. Morozova, Y. P. Sharaevsky, Y. A. Filimonov, Y. V. Khivintsev, S. L. Vysotsky, V. K. Sakharov, and E. S. Pavlov, *Phys.-Usp.* **58**, 1002 (2015).

⁵ T. Brächer, P. Pirro, and B. Hillebrands, *Phys. Rep.* **699**, 1 (2017).

⁶ T. Hula, K. Schultheiss, F. J. T. Goncalves, L. Körber, M. Bejarano, M. Copus, L. Flacke, L. Liensberger, A. Buzdakov, A. Kákay, *et al.*, arXiv preprint arXiv:2104.11491 (2021).

⁷ P. Pirro, V. I. Vasyuchka, A. A. Serga, and B. Hillebrands,

Nature Reviews Materials, 1 (2021).

⁸ Q. Wang, A. Samadeh, R. Verba, V. Lomakin, M. Mohseni, B. Hillebrands, A. V. Chumak, and P. Pirro, *NPJ Computational Materials* **6**, 1 (2020).

⁹ A. D. Boardman and S. A. Nikitov, *Phys. Rev. B* **38**, 11444 (1988).

¹⁰ G. T. Kazakov, A. V. Kozhevnikov, and Y. A. Filimonov, *Phys. Solid State* **39**, 288 (1997).

¹¹ J. M. Pereira Jr and M. G. Cottam, *J. Magn. Magn. Mater.* **258**, 329 (2003).

¹² R. N. Costa Filho, M. G. Cottam, and G. A. Farias, *Phys. Rev. B* **62**, 6545 (2000).

¹³ V. T. Synogach, Y. K. Fetisov, C. Mathieu, and C. E. Patton, *Phys. Rev. Lett.* **85**, 2184 (2000).

¹⁴ V. E. Demidov, S. O. Demokritov, K. Rott, P. Krzytsteczko, and G. Reiss, *J. Phys. D: Appl. Phys.* **41**, 164012 (2008).

¹⁵ G. A. Melkov, Y. V. Kobylanskiy, R. A. Slipets, A. V. Talalaevskij, and A. N. Slavin, *Phys. Rev. B* **79**, 134411 (2009).

- ¹⁶ H. Kurebayashi, O. Dzyapko, V. E. Demidov, D. Fang, A. J. Ferguson, and S. O. Demokritov, *Nat. Mater.* **10**, 660 (2011).
- ¹⁷ M. E. Zhitomirsky and A. L. Chernyshev, *Rev. Mod. Phys.* **85**, 219 (2013).
- ¹⁸ A. V. Sadovnikov, E. N. Beginin, M. A. Morozova, Y. P. Sharaevskii, S. V. Grishin, S. E. Sheshukova, and S. A. Nikitov, *Appl. Phys. Lett.* **109**, 042407 (2016).
- ¹⁹ A. V. Sadovnikov, S. A. Odintsov, E. N. Beginin, S. E. Sheshukova, Y. P. Sharaevskii, and S. A. Nikitov, *Phys. Rev. B* **96**, 144428 (2017).
- ²⁰ H. J. J. Liu, G. A. Riley, C. L. Ordóñez-Romero, B. A. Kalinikos, and K. S. Buchanan, *Phys. Rev. B* **99**, 024429 (2019).
- ²¹ R. Verba, V. Tiberkevich, and A. Slavin, *Phys. Rev. B* **99**, 174431 (2019).
- ²² D. V. Slobodianiuk, G. A. Melkov, K. Schultheiss, H. Schultheiss, and R. V. Verba, *IEEE Magn. Lett.* **10**, 1 (2019).
- ²³ S. Demokritov, D. V., O. Dzyapko, G. A. Melkov, A. A. Serga, A. A. Hillebrands, and A. N. Slavin, *Nature* **443**, 430 (2006).
- ²⁴ A. V. Chumak, A. A. Serga, and B. Hillebrands, *Nat. Commun.* **5**, 4700 (2014).
- ²⁵ J. Chen, J. Hu, and H. Yu, *ACS Nano* **15**, 4372 (2021).
- ²⁶ H. Yu, J. Xiao, and H. Schultheiss, *Phys. Rep.* **905**, 1 (2021).
- ²⁷ N. N. Dadoenkova, Y. S. Dadoenkova, I. L. Lyubchanskii, M. Krawczyk, and K. Y. Guslienko, *Phys. Status Solidi RRL* **13**, 1800589 (2019).
- ²⁸ M. G. Cottam and D. J. Lockwood, *Light scattering in magnetic solids* (Wiley, 1986).
- ²⁹ Z. Wang, H. Yuan, Y. Cao, Z.-X. Li, R. A. Duine, and P. Yan, *Physical Review Letters* **127**, 037202 (2021).
- ³⁰ B. Zhang, Z. Wang, Y. Cao, P. Yan, and X. Wang, *Phys. Rev. B* **97**, 094421 (2018).
- ³¹ R. Shindou, R. Matsumoto, S. Murakami, and J.-i. Ohe, *Phys. Rev. B* **87**, 174427 (2013).
- ³² I. Lisenkov, V. Tyberkevych, S. Nikitov, and A. Slavin, *Phys. Rev. B* **93**, 214441 (2016).
- ³³ A. Lara, V. Metlushko, and F. G. Aliev, *J. Appl. Phys.* **114**, 213905 (2013).
- ³⁴ F. Guo, L. M. Belova, and R. D. McMichael, *Phys. Rev. Lett.* **110**, 017601 (2013).
- ³⁵ J. Jorzick, S. O. Demokritov, B. Hillebrands, M. Bailleul, C. Fermon, K. Y. Guslienko, A. N. Slavin, D. V. Berkov, and N. L. Gorn, *Phys. Rev. Lett.* **88**, 047204 (2002).
- ³⁶ V. V. Kruglyak, P. S. Keatley, R. J. Hicken, J. R. Childress, and J. A. Katine, *J. Appl. Phys.* **99**, 08F306 (2006).
- ³⁷ M. Bailleul, D. Olligs, and C. Fermon, *Phys. Rev. Lett.* **91**, 137204 (2003).
- ³⁸ P. Gruszecki, J. Romero-Vivas, Y. S. Dadoenkova, N. N. Dadoenkova, I. L. Lyubchanskii, and M. Krawczyk, *Appl. Phys. Lett.* **105**, 242406 (2014).
- ³⁹ P. Gruszecki, Y. S. Dadoenkova, N. N. Dadoenkova, I. L. Lyubchanskii, J. Romero-Vivas, K. Y. Guslienko, and M. Krawczyk, *Phys. Rev. B* **92**, 054427 (2015).
- ⁴⁰ Z. Wang, B. Zhang, Y. Cao, and P. Yan, *Phys. Rev. Appl.* **10**, 054018 (2018).
- ⁴¹ A. B. Ustinov and B. A. Kalinikos, *Appl. Phys. Lett.* **90**, 252510 (2007).
- ⁴² A. B. Ustinov, E. Lähderanta, M. Inoue, and B. A. Kalinikos, *IEEE Magn. Lett.* **10**, 1 (2019).
- ⁴³ M. Song, K.-W. Moon, C. Hwang, and K.-J. Kim, *Phys. Rev. Appl.* **11**, 024027 (2019).
- ⁴⁴ R. D. McMichael, C. A. Ross, and V. P. Chuang, *J. Appl. Phys.* **103**, 07C505 (2008).
- ⁴⁵ P. Gruszecki, K. Y. Guslienko, I. L. Lyubchanskii, and M. Krawczyk, *Appl. Phys. Lett.* **118**, 062408 (2021).
- ⁴⁶ T. L. Gilbert, *IEEE Trans. Magn.* **40**, 3443 (2004).
- ⁴⁷ A. Vansteenkiste, J. Leliaert, M. Dvornik, M. Helsen, F. Garcia-Sanchez, and B. Van Waeyenberge, *AIP Adv.* **4**, 107133 (2014).
- ⁴⁸ B. A. Kalinikos and A. N. Slavin, *J. Phys. C: Sol. St. Phys.* **19**, 7013 (1986).
- ⁴⁹ D. D. Stancil and A. Prabhakar, *Spin Waves: Theory and Applications* (Springer, 2009).
- ⁵⁰ E. H. Lokk, *Phys.-Usp.* **51**, 375 (2008).
- ⁵¹ J. C. Slonczewski, *J. Magn. Mater.* **12**, 108 (1979).
- ⁵² H. Suhl, *J. Phys. Chem. Solids* **1**, 209 (1957).
- ⁵³ K. Y. Guslienko and A. N. Slavin, *J. Magn. Mater.* **323**, 2418 (2011).
- ⁵⁴ G. Gubbiotti, M. Conti, G. Carlotti, P. Candeloro, E. Di Fabrizio, K. Y. Guslienko, A. Andre, C. Bayer, and A. N. Slavin, *J. Phys. Condens. Matter* **16**, 7709 (2004).
- ⁵⁵ C. Bayer, J. Jorzick, B. Hillebrands, S. O. Demokritov, R. Kouba, R. Bozinoski, A. N. Slavin, K. Y. Guslienko, D. V. Berkov, N. L. Gorn, and K. M. P, *Phys. Rev. B* **72**, 064427 (2005).
- ⁵⁶ A. Lara, J. R. Moreno, K. Y. Guslienko, and F. G. Aliev, *Sci. Rep.* **7**, 5597 (2017).
- ⁵⁷ S. J. Hermsdoerfer, H. Schultheiss, C. Rausch, S. Schäfer, B. Leven, S.-K. Kim, and B. Hillebrands, *Appl. Phys. Lett.* **94**, 223510 (2009).
- ⁵⁸ Á. Papp, W. Porod, Á. I. Csurgay, and G. Csaba, *Sci. Rep.* **7**, 1 (2017).
- ⁵⁹ P. Gruszecki and M. Krawczyk, *Phys. Rev. B* **97**, 094424 (2018).
- ⁶⁰ C. R. Harris, K. J. Millman, S. J. van der Walt, R. Gommers, P. Virtanen, D. Cournapeau, E. Wieser, J. Taylor, S. Berg, N. J. Smith, R. Kern, M. Picus, S. Hoyer, M. H. van Kerkwijk, M. Brett, A. Haldane, J. F. del Río, M. Wiebe, P. Peterson, P. Gérard-Marchant, K. Sheppard, T. Reddy, W. Weckesser, H. Abbasi, C. Gohlke, and T. E. Oliphant, *Nature* **585**, 357 (2020).
- ⁶¹ “Discrete Fourier Transform (numpy.fft),” <https://numpy.org/doc/stable/reference/routines.fft.html>, accessed: 2021-04-21.